ACS NANO
Cite This: ACS Nano 2018, 12, 8060–8070
www.acsnano.org

ARTICLE

Solvent- and Wavelength-Dependent Photoluminescence Relaxation Dynamics of Carbon Nanotube sp^3 Defect States

Xiaowei He,[†,#] Kirill A. Velizhanin,[‡,#] George Bullard,[§] Yusong Bai,[§] Jean-Hubert Olivier,[§,○] Nicolai F. Hartmann,[†] Brendan J. Gifford,[‡,∥,⊥] Svetlana Kilina,[⊥] Sergei Tretiak,[†,‡] Han Htoon,[†] Michael J. Therien,[§] and Stephen K. Doorn*[,†]

[†]Center for Integrated Nanotechnologies, Materials Physics and Applications Division, Los Alamos National Laboratory, Los Alamos, New Mexico 87545, United States
[‡]Theoretical Division, Los Alamos National Laboratory, Los Alamos, New Mexico 87545, United States
[§]Department of Chemistry, French Family Science Center, Duke University, Durham, North Carolina 27708, United States
[∥]Center for Nonlinear Sciences, Los Alamos National Laboratory, Los Alamos, New Mexico 87545, United States
[⊥]Department of Chemistry and Biochemistry, North Dakota State University, Fargo, North Dakota 58108, United States

Supporting Information

ABSTRACT: Photoluminescent sp^3 defect states introduced to single wall carbon nanotubes (SWCNTs) through low-level covalent functionalization create new photophysical behaviors and functionality as a result of defect sites acting as exciton traps. Evaluation of relaxation dynamics in varying dielectric environments can aid in advancing a more complete description of defect-state relaxation pathways and electronic structure. Here, we exploit helical wrapping polymers as a route to suspending (6,5) SWCNTs covalently functionalized with 4-methoxybenzene in solvent systems including H_2O, D_2O, methanol, dimethylformamide, tetrahydrofuran, and toluene, spanning a range of dielectric constants from 80 to 3. Defect-state photoluminescence decays were measured as a function of emission wavelength and solvent environment. Emission decays are biexponential, with short lifetime components on the order of 65 ps and long components ranging from around 100 to 350 ps. Both short and long decay components increase as emission wavelength increases, while only the long lifetime component shows a solvent dependence. We demonstrate that the wavelength dependence is a consequence of thermal detrapping of defect-state excitons to produce mobile E_{11} excitons, providing an important mechanism for loss of defect-state population. Deeper trap states (i.e., those emitting at longer wavelengths) result in a decreased rate for thermal loss. The solvent-independent behavior of the short lifetime component is consistent with its assignment as the characteristic time for redistribution of exciton population between bright and dark defect states. The solvent dependence of the long lifetime component is shown to be consistent with relaxation via an electronic to vibrational energy transfer mechanism, in which energy is resonantly lost to solvent vibrations in a complementary mechanism to multiphonon decay processes.

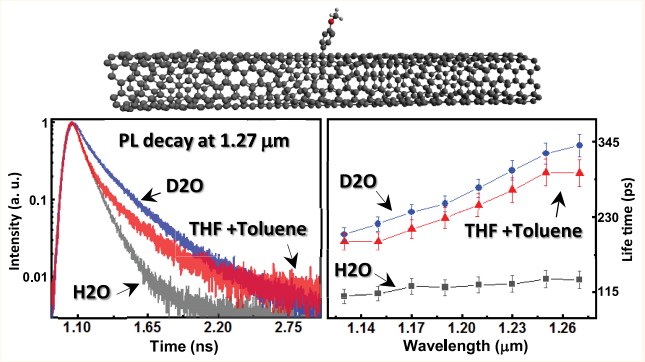

KEYWORDS: *single wall carbon nanotubes, exciton, sp^3 defects, photoluminescence decay, relaxation dynamics, thermal detrapping, electronic-to-vibrational energy transfer*

Low-level covalent functionalization of semiconducting single-wall carbon nanotubes (SWCNTs) by oxygen,[1] aryl,[2] and alkyl groups,[3] with the latter two classes creating sp^3 defects, introduces new photoluminescent emitting states that are strongly red-shifted from the emission commonly observed from the nanotube band-edge E_{11} exciton state.[4] In addition to being the source of new photophysical behaviors, these states are drawing significant interest as the basis for emerging functionality, with possibilities including enhanced sensing and imaging,[1,5,6] photon upconversion,[7−9]

Received: April 18, 2018
Accepted: July 11, 2018
Published: July 11, 2018

DOI: 10.1021/acsnano.8b02909
ACS Nano 2018, 12, 8060–8070

and potential to act as room-temperature single photon emitters.[10,11] Many of these behaviors arise due to localization of the diffusive band-edge exciton at the defect site.[12−15] The localized exciton adopts a modified electronic structure defined by the molecular dopant forming the defect.[1,2,15−18] Localization also modifies photoluminescence (PL) saturation behavior.[15,18,19] A particularly important signature of the exciton localization at defect sites is that, because the exciton is no longer free to diffusively sample PL quenching sites along the length of the carbon nanotube,[20] its PL lifetime is significantly extended.[10−12,14]

The photoluminescence dynamics of the defect states is a significant determining factor in the enhanced PL quantum yield observed from these states.[12] The observation of an increased defect-state PL lifetime as SWCNT diameter decreases (and emission energy increases) has pointed to the primary nonradiative decay mechanism being that of multiphonon decay (MPD),[14] since the MPD rate will decrease as the number of phonons required to bridge the energy gap increases.[21] While suggested by Perebeinos and Avouris in 2008,[21] such a mechanism had been masked by diffusive exciton quenching, and only became apparent due to localization at defect sites.[14] Defect-state decay at room temperature is found to be biexponential,[11,14] indicating that relaxation may involve two levels within the defect-state manifold.[14] Temperature-dependent spectra[12] and density functional theory (DFT) modeling[22] suggest that these two states are likely to be a bright (i.e., optically allowed) emitting state and another that is dark (i.e., optically forbidden), with energy ordering depending on the specific local molecular structure associated with the defect. With the two decay components being similar in time scale and in weighting, a model has been proposed for which the shorter component corresponds to a time scale for redistribution of the populations within the two energetically closely spaced defect states, while the long-time component corresponds to the time scale for relaxation of the entire defect-state manifold back to the ground state (see Figure 1a).[14] The biexponential relaxation behavior thus provides additional information on the electronic structure associated with the defects. In addition to relaxation to the ground state, thermal detrapping of defect-state excitons to produce mobile E_{11} excitons (as observed in the photon-upconversion process)[7] provides another possible channel for loss of defect-state population (Figure 1a), but requires further evaluation.

A full mechanistic understanding of defect-state relaxation is not yet available, in part due to samples being limited to those primarily generated in aqueous environments (due to limitations in functionalization chemistry and nanotube suspension methods). Access to a broader range of solvents would allow probing of how dielectric environment and specific solvent-SWCNT interactions impact relaxation, further enhancing our understanding of decay mechanism. Here we present a route to polymer wrapping (Figure 1b) of functionalized SWCNTs that allows for exchange of the nanotubes from an aqueous environment into a range of six different solvents spanning dielectric constants from 80 (water) to 3 (toluene). We obtain PL lifetime data for methoxybenzene-functionalized (6,5) SWCNTs as a function of the solvent environment, and as a function of defect-state emission wavelength. We observe an increase in PL lifetime as defect-state emission wavelength increases, which is attributed primarily to the effects of thermal detrapping and allows an

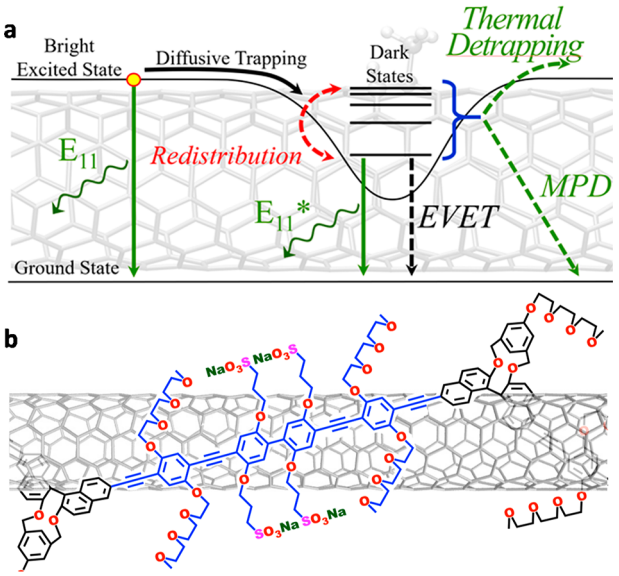

Figure 1. (a) Depiction of defect state formation and relaxation processes. Initial band-edge exciton may emit light (E_{11}) or is diffusively trapped at defect site. Possible defect-state relaxation pathways include population redistribution between bright emitting and dark states (red dashed arrow), radiative relaxation to emit a photon from the E_{11}* defect state (green vertical arrow), and nonradiative processes (depicted as dashed arrows) including multiphonon decay (MPD), electronic-to-vibrational energy transfer to solvent (EVET), and thermal detrapping to regenerate the band-edge exciton. (b) Schematic illustrating single-handed helical wrapping of a SWCNT surface with an [arylene]ethynylene polymer.

assessment of the relative impact such detrapping has on overall defect-state population loss. We also find that, for the long lifetime component, decay times increase as dielectric constant of the solvent decreases. Using quantum chemical calculations and condensed matter theory models, we demonstrate this observation to be a consequence of an electronic-to-vibrational energy transfer (EVET) mechanism for relaxation. In contrast, the short component is insensitive to a change in solvent. The latter observations are shown to be consistent with initial assignments of the short component being due to a redistribution of exciton population among the different states of the defect-state manifold, while the long component is due to overall relaxation to the ground state.[14]

RESULTS AND DISCUSSION

While dielectric effects on SWCNT optical properties have been studied at the single nanotube level,[23,24] similar ensemble level studies are more problematic. The most common methods for generating solution phase samples typically involve the use of agents including surfactants[25] or DNA[26] to generate aqueous suspensions. Alternatively, wrapping SWCNTs with polyfluorene polymers provides an efficient route to toluene-based suspensions.[27] In each case, subsequent SWCNT exchange into a broad range of organic solvents is not possible. The use of [arylene]ethynylene polymers as wrapping agents, in conjunction with phase-transfer catalysts, however, presents an effective route for exchanging aqueous SWCNTs into stable organic suspensions in several solvent systems.[28−33] To study the environment dependence of exciton dynamics from sp^3 defects in SWCNTs, we followed the strategy of first functionalizing SWCNTs with 4-methoxybenzene (in aqueous

DOI: 10.1021/acsnano.8b02909
ACS Nano 2018, 12, 8060−8070

1% sodium dodecyl sulfate (SDS)), followed by exchange of the surfactant *via* wrapping with an [arylene]ethynylene polymer (specifically, poly[2,6-{1,5-bis(3-propoxysulfonic acid sodium salt)}naphthylene]ethynylene (S-PBn(b)-Ph_4), see Methods). Purification of the assembled S-PBn(b)-Ph_4-[(6,5) SWCNT] superstructure by gel permeation chromatography removes surfactants (SDS) and unbound polymer, rendering a sample that displays a constant and periodic single-stranded, self-assembled helical wrapping (see Figure 1b and also Supporting Information Figure S1) that leaves ~80% of the SWCNT surface exposed to the solvent environment,[33] while also endowing SWCNT solubility in a wide-range of organic solvents. Importantly, the morphology of the semiconducting polymer-wrapped SWCNT superstructure and the electronic structure of the polymer remain unchanged by changes in solvent dielectric,[28] providing an ideal platform for elucidating and monitoring SWCNT spectroscopic features.[34] Specifically, this system offers an excellent template to study the environmental influence on PL dynamics of excitons localized at aryl sp^3 defects in SWCNTs. The aqueous polymer-wrapped functionalized SWCNTs were ultimately exchanged into a series of organic solvent systems for optical studies. (See Methods for details.)

Solvent-Dependent Defect-State PL Spectra. In this work, 4-methoxybenzene-functionalized S-PBn(b)-Ph_4-[(6,5) SWCNT] superstructures were dispersed in H_2O, D_2O, methanol, dimethylformamide (DMF), thetrahydrofuran (THF) and a toluene (80%)/THF (20%) mixture, with respective static dielectric constants of 80 (H_2O and D_2O), 36.7, 32.7, 7.58, and 3. Shown in Figure 2 are the room temperature ensemble PL spectra of the functionalized (6, 5) SWCNTs, for each solvent system. Three PL peaks are observed in each spectrum, corresponding to E_{11} emission (1013 nm in H_2O), and two defect-state emission peaks labeled as E_{11}^* and the significantly weaker E_{11}^{*-} (at 1162 and 1283 nm, respectively, in H_2O). The two defect-state emission bands are understood to arise due to multiple binding configurations of the aryl dopant being allowed on the nanotube structure, effectively creating the possibility of chemically distinct defect sites occurring on the SWCNT surface, each with a separately defined electronic structure and emission energy[18] (see Supporting Information Tables S2 and S3). We note that, for S-PBn(b)-Ph_4 wrappings, the E_{11} emission peak is red-shifted from that of (6,5) SWCNT in aqueous sodium deoxycholate (DOC) suspensions (typically observed at ~985 nm), as the result of significant $\pi-\pi$ interactions between the polymer backbone and the nanotubes.[33]

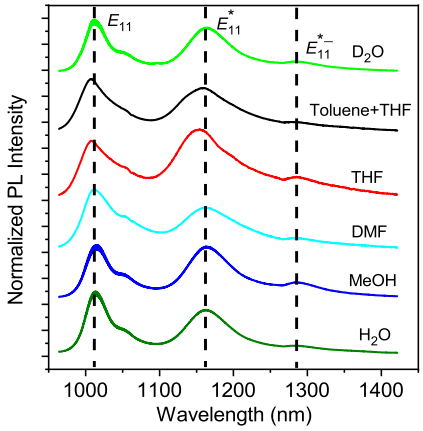

Figure 2. Ensemble PL spectra of 4-methoxybenzene-functionalized S-PBn(b)-Ph_4-[(6,5) SWCNT] superstructures, suspended in six different solvent systems. Peaks due to band-edge exciton emission (E_{11}) and defect-state emission (E_{11}^* and E_{11}^{*-}) are labeled. Intensities are normalized to the E_{11} peak in each spectrum. Spectra are offset for clarity.

Interestingly, the PL spectra are nearly identical for all six solvents. Particularly, the relative intensity of both E_{11}^* and E_{11}^{*-} bands with respect to the E_{11} peak vary only moderately between solvents. We note that the relative intensities across the solvent choices are directly comparable because the same source of functionalized SWCNTs was used in all cases. Therefore, defect density is unchanged across the solvents. The minor variability in relative intensities indicates that defect-state oscillator strength is insensitive to these solvent environments. Additionally, emission wavelengths for both defect-state peaks are nearly unchanged as solvent varies, with deviations within 10 nm (Figure 2 and Supporting Information Table S1). Such experimental results are consistent with theoretical studies showing the defect-state oscillator strengths and emission energies should have only a limited dependence on the external environment, as a consequence of the relatively small permanent dipole introduced by functionalization at the defect site.[18,35] Despite the minor sensitivity of the spectral response to solvent changes, solvent environment may still be expected to have an impact on defect-state relaxation dynamics through specific solvent-nanotube interactions and impacts on multiphonon decay mechanisms. Therefore, we also performed PL lifetime measurements on the functionalized SWCNTs in different solvents to reveal environmental influence on the exciton dynamics.

PL Lifetime Dependence on Defect-State Emission Wavelength. As reported previously,[14] we find that the defect-state PL decays in all solvents are biexponential, with a short component (τ_s) having decay times of tens of ps and a long component (τ_l) having decay times of hundreds of ps (see Figure S2, Supporting Information). The two decay components are plotted as a function of defect-state emission wavelength and for each solvent system in Figure 3. As noted above and as depicted in Figure 1a, the fast decay (τ_s) in the biexponential relaxation dynamics corresponds to the redistribution or scattering of the excitonic population between the bright and dark trapped exciton states, shown by the red dashed arrow in Figure 1a.[14] Importantly, the fast initial PL decay does not represent a fast exciton recombination, but instead is due to rapid equilibration of the initially trapped exciton population across the bright and dark trap-state manifold. Once the exciton population is equilibrated between the bright and dark localized states, the relatively slow recombination of the trapped excitons via various channels (see below and Figure 1a) determines the decay time of the slow component (τ_l). We first discuss the short and long decay time dependences on emission wavelength.

Both the short (τ_s, Figure 3a) and long (τ_l, Figure 3b) decay components increase as longer emission wavelengths are probed. Interestingly, decay times measured across a series of different SWCNT chiralities show an opposing trend to that displayed in Figure 3, with PL lifetime decreasing as chirality-dependent emission energies decreased.[14] This behavior was understood as arising from a multiphonon decay (MPD) process (Figure 1a), for which the MPD rate decreases

DOI: 10.1021/acsnano.8b02909
ACS Nano 2018, 12, 8060−8070

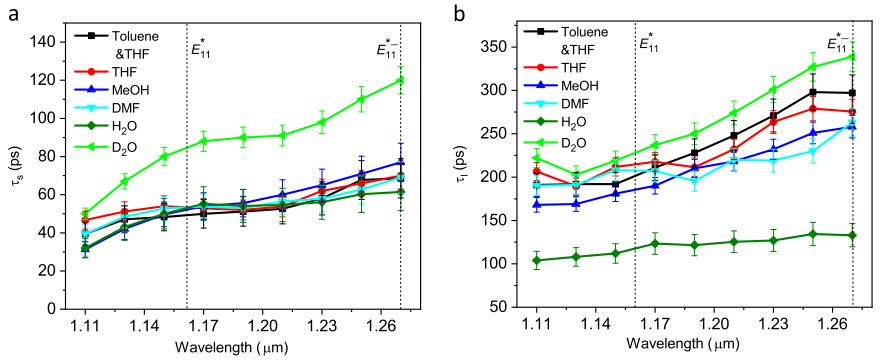

Figure 3. (a) Short (τ_s) and (b) long (τ_l) PL lifetime components for defect-state PL decay as a function of wavelength for six different solvent systems. Data points are shown as symbols, with line added as a guide to the eye. All excited-state dynamical data examine solvent-dispersed 4-methoxybenzene-functionalized S-PBn(b)-Ph$_4$-[(6,5) SWCNT] superstructures.

approximately exponentially with the number of phonons required to bridge the chirality-dependent electronic gap.[21] In contrast, the wavelength dependence in Figure 3 indicates that, for a given SWCNT chirality, a competing process coexists, with an opposing energy dependence, but likely occurs on a similar time scale as MPD.

We note that as emission is probed across the wavelength range displayed for the defect states in Figures 2 and 3, different emitting states, E_{11}* at ∼1162 nm and E_{11}*$^-$ at ∼1283 nm (see Table S1 in the Supporting Information), arising from the different available dopant binding configurations,[18,35] are sampled. Variation in relaxation behavior with emission wavelength therefore may be tied to differing behavior of the individual states. We consider a number of possible origins for these differences. One candidate, tied to nonradiative decay, is that each state may couple differently to phonons in the MPD process.[21] A particular measure of exciton−phonon coupling is vibrational reorganization energy, which reflects the deformation of the nanotube structure that occurs upon exciton trapping at the defect site, with the magnitude being determined by the degree of coupling between the localized exciton and the related SWCNT phonons. This reorganization energy has been found previously to be on the order of 100 meV for defect states.[22] While variations in exciton−phonon coupling between defect states might explain some of the wavelength dependence observed in the decay times, DFT calculations show that this coupling is expected to be similar for each binding configuration (see Methods, and Figure S3 and Table S2 in the Supporting Information), owing to a similarity of phonon modes coupled to the electronic degrees of freedom for each of the different binding configurations. Such an explanation of the observed lifetime increase at longer wavelengths is therefore unlikely.

Alternatively, we consider a possible wavelength dependence in the radiative recombination rate, given by $k_r \propto (\hbar\omega)^3|d|^2$,[36] where $\hbar\omega$ is the transition energy and d is the magnitude of the transition dipole. Through DFT calculations (see Methods and ref 22), we find that the defect-trapped exciton wave function becomes more strongly localized as trapping energy increases. This is the case as one moves to progressively more red-shifted defect emitting states (Figure 1a). As a result (see Section I in the Supporting Information), the magnitude of the associated radiative transition dipole moment negatively correlates with the trapping energy (i.e., the stronger the trapping, the lower the transition dipole moment and thus k_r, see Table S2 in Supporting Information). Beyond the effects of localization on the radiative recombination rate, the decrease in emission energy ($\hbar\omega$) itself also contributes to an expectation of decreased radiative rate. These two factors will thus both result in longer PL lifetimes at longer emission wavelength, which qualitatively agrees with the trends seen in Figure 3a and b. However, DFT calculations suggest that the magnitude of the PL lifetime for the systems of interest is expected to be on the order of a nanosecond for a trapped exciton (Table S2, Supporting Information), similar to expectations for the radiative lifetime of the E_{11} state,[37,38] while the apparent lifetimes in Figure 3 are at least an order of magnitude smaller. Therefore, the radiative recombination channel will contribute nearly negligibly to the observed exciton relaxation lifetimes, and so the wavelength dependence of the radiative lifetime cannot be the source of the apparent wavelength dependence in Figure 3.

As a final possibility, it was suggested in ref 14 that another nonradiative decay channel could be phonon-assisted thermal detrapping[22] (evident in photon upconversion),[7] which produces free E_{11} excitons that decay quickly (∼10−20 ps) through efficient diffusive sampling of quenching centers found on the SWCNT surface.[14] This process is schematically shown in Figure 1a by the curved green arrow. We assume the rate of thermal detrapping in the Arrhenius form $k_{dt} = A\,e^{-E_a/k_BT}$,[22] where the activation energy E_a is taken to be the energy difference between the free and trapped exciton states (0.157 and 0.258 eV for the E_{11}* and E_{11}*$^-$ PL peaks in Figure 2, respectively). By transition state theory, one can approximate the pre-exponential factor as $A = k_BT/h$, where h is Planck's constant. At room temperature, this results in $A \approx 6 \times 10^{12}\ s^{-1}$, and yields detrapping times on the order of $\tau_{dt} = \frac{1}{k_{dt}} \sim 100 - 300\,ps$ for the E_{11}* transition, and in the several nanoseconds range for the E_{11}*$^-$ transition. The large uncertainty originates from the exponential sensitivity of the detrapping rate on the energies of transitions.

The resulting magnitude of the detrapping times is seen to be in qualitative agreement with the results of measurements in Figure 3b. For all solvents, excluding water, lifetime changes from ≈200 to ≈300 ps when the wavelength changes from 1160 to 1280 nm (Table S1, Supporting Information), the spectral region corresponding to defect-state PL for the different available dopant binding configurations.[18,35] We hypothesize that water is an exception because nonradiative recombination of trapped SWCNT excitons in water is

DOI: 10.1021/acsnano.8b02909
ACS Nano 2018, 12, 8060−8070

dominated by the so-called EVET, discussed in detail in the next section. These data therefore suggest that the thermal detrapping defines an important deactivation channel for trapped defect-state excitons, which explains the lifetime-vs-wavelength behavior in Figure 3. Such a process is also consistent with previous reports of photon up-conversion[7] and an increase in defect-state PL intensity as T decreases,[12,22] which is also accompanied by an increased PL lifetime.[10] Furthermore, our results indicate that thermal detrapping and MPD are the dominant channels of nonradiative decay in all solvents (except H_2O). Quantitatively, the decay lifetime of the long PL component (Figure 3b) can be represented by $\frac{1}{\tau_l} = \frac{1}{\tau_{dt}} + \frac{1}{\tau_{MPD}} + k_{other}$, where k_{other} is the cumulative rate constant of all contributing processes other than detrapping or MPD that includes, for example, radiative recombination. For all solvents except H_2O, k_{other} is nearly negligible, resulting in lifetimes for different solvents being nearly superimposed in Figure 3b. For water, k_{other} becomes substantial due to efficient EVET (see below).

The lifetime of the short component (Figure 3a) is given by $\frac{1}{\tau_s} = \frac{1}{\tau_{rd}} + \frac{1}{\tau_l}$, where τ_{rd} is the time constant for redistribution of the bright and dark defect states.[14] Here we assume that τ_{dt}, τ_{MPD}, and k_{other} do not depend on whether an exciton resides in the bright or dark trapped state. The rate of redistribution is not expected to be strongly dependent on emission wavelength, since the scale of the associated bright-dark energy splitting within the defect-state manifold is significantly less than that for detrapping energy. Indeed, the lifetime of the short component changes only from ≈55 to ≈65 ps over the wavelength range of 1160−1280 nm. This variation can be reproduced approximately by assuming constant τ_{rd} = 80 ps and that τ_l varies from 200 to 300 ps within the same wavelength range, in agreement with Figure 3b. Collectively, these data indicate that the two main contributions to the long component decay rate, $1/\tau_l$, in Figure 3b are MPD and thermal detrapping, with the latter providing the apparent lifetime-vs-wavelength dependence highlighted in Figure 3b. The short component lifetime incorporates the same exciton recombination channels, but the redistribution process shortens the apparent lifetime, since $\frac{1}{\tau_s} = \frac{1}{\tau_{rd}} + \frac{1}{\tau_l} > \frac{1}{\tau_l}$.

Defect-State PL Lifetime Dependence on Solvent. Inspection of Figure 3 also reveals a contrast in solvent dependent behaviors between the short and long components of the PL decay. While the long component shows significant variation with solvent (Figure 3b), the magnitude of the short component, with the exception of D_2O, is insensitive to specific solvent (Figures 3a and 4). As highlighted in Figure 4, τ_s is nearly constant across a wide range of solvent dielectric response. This is consistent with assignment of τ_s as reflecting the rate of redistribution between bright and dark states of the trapped exciton. Scattering between the states is unlikely to be dependent on solvent dielectric. The stark difference in τ_s for D_2O in comparison to H_2O does, however, indicate an isotopic dependence that may reflect some involvement of solvent vibrational modes in the scattering process.

The long decay component shows a much stronger dependence on the solvent (Figure 3b). Empirically, there is a strong negative correlation between the magnitude of the solvent static dielectric constant and τ_l (Figure 5a), particularly when evaluated at the longest defect-state emission wavelengths (1250 nm). Interestingly, a strong isotopic dependence

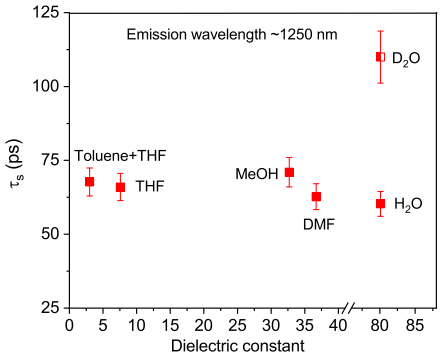

Figure 4. Short PL lifetime component (τ_s) as a function of solvent dielectric constant for the six labeled solvents. Data taken for PL emission centered at 1250 nm.

in the behavior is also evident, with the lifetime in D_2O being twice that found for H_2O. As with the wavelength-dependent behavior discussed above, it is not likely that the solvent dependence has its origin in radiative relaxation, since the associated 10-fold longer time scale will not impact the observed decays. Furthermore, the radiative rate is expected to show only mild sensitivity to the dielectric range studied here (see the Supporting Information). The solvent dependence must therefore also originate in nonradiative relaxation processes. The empirical correlation we show between lifetime and static dielectric constant in Figure 5a may be useful for a quick determination of how solvent may impact defect-state dynamics and for developing practical strategies for tuning environmental interactions. However, it does not provide mechanistic insight, does not account for the long lifetime observed in D_2O, and is insufficient for explaining the more complex lifetime behavior observed at intermediate emission wavelengths (Figure 3b). We address these issues by developing a model based on EVET for relaxation of the defect states.

It has been shown previously that a solvent-to-solvent variation in exciton relaxation rates in colloidal nanosystems could be explained by an EVET process.[39,40] More specifically, polar solvents (e.g., water, methanol) often have combination vibrational bands with phonon energies up to ∼1 eV, so that an electronic excitation of a nanosystem (e.g, semiconductor quantum dot, SWCNT) can recombine nonradiatively by transferring energy to the solvent via Förster resonance energy transfer (FRET). We find that such a process, shown by the dashed vertical black arrow in Figure 1a, can explain the observed solvent dependence in τ_l, and particularly account for the large difference in behavior between H_2O and D_2O.

The magnitude of the EVET rate is linearly proportional to the imaginary part of the dielectric function, or, equivalently, to the absorption coefficient of the solvent at the frequency corresponding to the exciton transition.[39,40] Solvent absorption spectra in the range of the defect-state emission are shown in Figure 5b. We focus first on the H_2O/D_2O behavior. The absorption coefficient of water (dark green line, Figure 5b) is universally significantly larger than that of D_2O (light green line) in this spectral region. This is due to the pronounced isotopic red shift of all the characteristic rotational and vibrational modes of D_2O relative to H_2O. Such a large mismatch of absorption coefficients, and, therefore, of the EVET rates, explains qualitatively why the lifetime of the long component is so different for these two solvents.

DOI: 10.1021/acsnano.8b02909
ACS Nano 2018, 12, 8060−8070

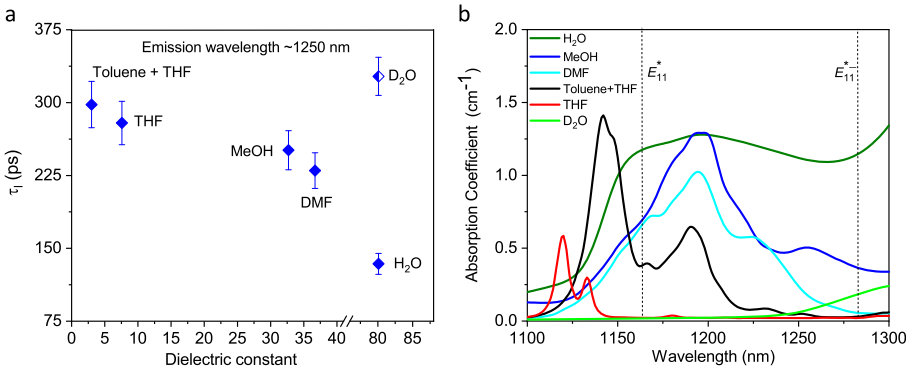

Figure 5. (a) Long PL lifetime component (τ_l) as a function of solvent dielectric constant for the six labeled solvents. Data taken for PL emission centered at 1250 nm. (b) Near-infrared absorption spectra for six solvent systems, each obtained in a 1 cm path length cuvette.

Quantitatively, the EVET rate Γ for the relaxation of the trapped exciton in SWCNTs is (see the Supporting Information for derivation and discussion)

$$\Gamma = \left(\frac{R_s}{R_x}\right)^2 \Gamma_{pd} \tag{1}$$

where R_s is the solvation radius for the SWCNT and R_x is the characteristic radius of the exciton localization. The EVET rate Γ_{pd} in the point dipole approximation is

$$\Gamma_{pd} = \frac{d^2}{R_s^3}\frac{4\epsilon_s''}{3\epsilon_s'^2} \tag{2}$$

and the factor of $(R_s/R_x)^2$ in eq 1 corrects Γ_{pd} by accounting for the finite extent of the transition dipole (see the Supporting Information). The complex dielectric function of the solvent, at the frequency corresponding to the energy of the transition, is $\epsilon_s = \epsilon_s' + i\epsilon_s''$. The following parameters are assumed: the characteristic value of the trapped exciton transition dipole is d = 38 D (Table S2, Supporting Information), and the solvation radius is $R_s \approx 0.7$ nm.[41,42] The real part of the dielectric function for H_2O and D_2O at optical frequencies is almost identical ($\epsilon_s' = \epsilon_{H_2O}' = \epsilon_{D_2O} \approx 1.75$ at λ = 1160 nm) and is only weakly wavelength-dependent.[43] The absorption coefficient for H_2O and D_2O at λ = 1160 nm are $\alpha_{H_2O} \approx 1.152$ cm^{-1} and $\alpha_{D_2O} \approx 0.017$ cm^{-1} (Figure 5b). The absorption coefficients are converted to the imaginary part of the dielectric function as $\epsilon_s'' = \alpha\frac{\lambda}{2\pi}\sqrt{\epsilon_s'}$ to produce $\epsilon_{H_2O}'' = 2.7 \times 10^{-5}$ and $\epsilon_{D_2O}'' = 4.1 \times 10^{-7}$. The resulting point-dipole EVET lifetimes, $1/\Gamma_{pd}$, are ≈21 ps and ≈1.4 ns for water and heavy water, respectively. Equation 1 accounts for the extended nature of the transition dipole and yields the final EVET lifetimes of 170 ps and 10 ns for water and heavy water, respectively, when the "radius" of the trapped exciton is taken to be $R_x \approx 2$ nm.[18]

The above estimates suggest that the EVET lifetime for D_2O is expected to be almost 2 orders of magnitude longer than that of H_2O, and also much longer than those for the MPD and thermal detrapping processes (see above). Therefore, one can neglect the EVET relaxation channel for D_2O, and it is reasonable to assume that the only difference between exciton relaxation in D_2O and water is the EVET channel, so that

$$\frac{1}{\tau_l(H_2O)} = \frac{1}{\tau_{EVET}(H_2O)} + \frac{1}{\tau_l(D_2O)} \tag{3}$$

We take values of $\tau_l(D_2O) \approx 220$ and 330 ps (Figure 3b) at wavelengths of 1160 and 1260 nm, respectively. With $\tau_{EVET}(H_2O)$ = 170 ps estimated above, one obtains $\tau_l(H_2O) \approx 96$ and 112 ps at the same two wavelengths. These values agree well with the actual experimental values for $\tau_l(H_2O)$ in Figure 3b, especially considering the level of approximations used to obtain eq 1.

To discuss behavior in the other solvents represented in Figure 3, we first consider τ_l in the long-wavelength range. This is the regime in which the effects of thermal detrapping are reduced, and also where the solvent absorbance varies the least with wavelength. For wavelengths ~1250−1280 nm, the absorption coefficient is seen to be the largest for water, followed by methanol and DMF whose absorption coefficient is a factor of ~2−3 lower, with THF and toluene being least absorptive. This qualitatively agrees with the lifetime trends of Figure 3b, where methanol and DMF display the shortest τ_l of all the solvents except H_2O. More quantitatively, lowering the EVET rate in eq 3 by a factor of 3 from that of H_2O (reflecting the corresponding change in absorption coefficient) yields $\tau_l \approx$ 230 ps, close to the lifetime values for methanol and DMF in Figures 3b and 5a. At this point, it is useful to comment on the pronounced negative correlation between the static dielectric function and τ_l, Figure 5a. As is clear from the above discussion, the static dielectric function is not directly related to the EVET, which is sensitive to the dynamic (i.e., vibrational) properties of the solvent. However, strong EVET coupling (i.e., large absorption coefficient in Figure 5b) in the considered solvents originates from the presence of high-frequency IR-active vibrations. Such IR-active vibrational modes are typically present in molecules possessing large static dipole moments. In turn, the ability to reorient this dipole moment in an external electric field is what results in a large static dielectric permittivity. This is the reason for the correlation in Figure 5a, which effectively establishes the magnitude of the static dielectric constant as a proxy for the EVET efficiency.

At shorter wavelengths (1100−1200 nm), the general trend with solvent is somewhat preserved in Figure 3b: H_2O consistently has the shortest τ_l, methanol and DMF typically have the shortest τ_l values of the organic solvents, and D_2O consistently displays the longest lifetime. There are specific points in the spectral response (e.g., near 1150 nm), however, at which lifetime behavior is more scrambled. These behaviors can be tied to the more complex structure of the solvent spectra in this region. From eq 1, the EVET time scales, and therefore defect-state PL lifetimes (Figure 3b), are expected to

DOI: 10.1021/acsnano.8b02909
ACS Nano 2018, 12, 8060−8070

be inversely proportional to the absorption coefficient in Figure 5b. Such an exact correspondence, however, is not the case. For example, at λ = 1190 nm the H_2O and methanol absorption coefficients are very close. However, τ_l, and therefore the EVET rate, for these two solvents remains significantly different.

One source of these discrepancies is likely due to dynamic change in defect-state energies on time scales faster than the EVET rate. The observed line width of defect-state emission for single defects on single carbon nanotubes (20−50 meV)[11] is partially due to transient changes in exciton−phonon coupling and solvent structure at the nanotube surface[44] that can occur on time scales (∼ps) shorter than the characteristic EVET rates. These *dynamic* changes can alter both the effective magnitude of R_s (eq 1) and defect-state energy, thus impacting its energy overlap with the solvent absorption. The effect diminishes the impact of sharp features of the solvent absorption spectrum so that, for example, the strong but narrow absorption maximum of methanol at λ = 1190 nm (Figure 5b) does not increase the observed EVET rate to match that of water. Unlike the other solvents, the water absorption in Figure 5b is consistently high and essentially uniform in the spectral window between the E_{11}^* and E_{11}^{*-} transitions. Therefore, dynamic averaging of energy overlap is not expected to strongly affect exciton relaxation in water. This also explains why EVET in water is much more effective than for other solvents, effectively generating a pronounced absorptive gap between H_2O and all other solvents over the wavelength range chronicled in Figure 3b.

The above discussion also neglects any specific interactions that may occur between solvent and defect site. We note that eq 1 implicitly treats the solvent as a continuum medium without accounting for such specific interactions. However, the static dipole associated with the functional group[13,45] can enhance interactions with the solvent molecules that may increase solvent-exciton coupling, while also making the effective solvation radius R_s in eqs 1 and 2 somewhat solvent-dependent.

Solvent Dependence of Decay Component Amplitudes. The relative amplitudes of the decay components extracted from biexponential fits to the defect-state PL decay (see Methods) provide additional information on relaxation mechanisms and defect-state electronic structure. The dependence of the amplitudes of the long PL decay components on the emission wavelength for different solvents is shown in Figure 6. Except for H_2O, all amplitudes are relatively the same for each solvent system and increase in weighting as defect-state emission wavelength increases. Weighting of the long decay component in H_2O remains nearly constant across the emission wavelength range and is significantly lower than that for the other solvents.

We analyze this behavior within a simplified model that consists of a single bright state and $n > 1$ degenerate dark states (Figure 1a). Of these states, the bright state is the lowest energy, as suggested by DFT calculations (Table S3 and Figure S5, Supporting Information). This model is described in detail in the Supporting Information (section III). We first consider the case of weak EVET, relevant for all solvents except H_2O. Under these conditions, as noted above, the redistribution within the defect-state manifold is significantly faster than the subsequent exciton recombination, which is reflected in the factor of ∼4−5 fold difference between short and long component lifetimes in Figure 3. The defect bright and dark

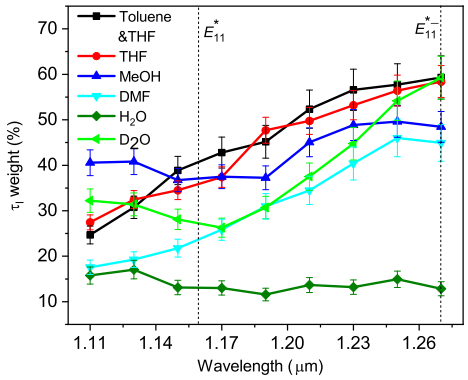

Figure 6. Relative weighting of the long lifetime component for biexponential PL decay fits (see Methods) as a function of defect-state emission wavelength for six different solvent systems. Data points are shown as symbols, with lines added as a guide to the eye. All PL data were acquired from solvent-dispersed 4-methoxybenzene-functionalized S-PBn(b)-Ph$_4$-[(6,5) SWCNT] superstructure samples. Note that weighting for the short lifetime component will be 1 minus the long lifetime weighting.

states thus rapidly equilibrate and the bright state population is given by $p_b^{eq} = 1/(1 + n\, e^{-\epsilon/k_BT})$, where n is the degeneracy of the dark states and ϵ is the bright-dark energy splitting. It is shown in the Supporting Information (section III) that the normalized amplitude of the long PL component in this case is $A_l = p_b^{eq}/(1 - p_d)$, where p_d is the initial (i.e., immediately after trapping) total population of dark states.

As noted above, the wavelength variation of the lifetime components is related to sampling different emitting states, E_{11}^* at ∼1160 nm and E_{11}^{*-} at ∼1280 nm, arising from the different available dopant binding configurations.[18,35] Of the possible binding configurations, those with the larger trapping energy, and therefore longer emission wavelengths, have a larger difference in energies between the lowest bright and dark states (see Supporting Information Table S3 and Figure S5 for relative ordering and energy separations of bright and dark defect states). This, in turn, means that p_b^{eq} is larger for the defect with larger trapping energy, thus producing larger amplitude A_l. This agrees with the data shown in Figure 6.

In the case of H_2O, the EVET exciton recombination channel dominates over thermal detrapping. In this case, the recombination rate constant k can become larger than the redistribution rate constant k_{rd}, and the amplitude of the long PL component becomes (see Supporting Information section III for the derivation)

$$A_l = n\, e^{-\epsilon/k_BT}\frac{k_{rd}^2}{k^2} + \frac{k_{rd}(k + k_0 - n\, e^{-\epsilon/k_BT}k_{rd})}{k^2(1 - p_d)}p_d \qquad (4)$$

Importantly, both terms in this expression decay with k, so that A_l can become small if k is large. Physically, this is reasonable because an exciton scattered into the bright defect state from the dark ones via redistribution recombines rapidly via combined EVET and MPD. Therefore, the instantaneous population of the bright trapped state is small, resulting in a small A_l. This result agrees with the generally small amplitude of the long PL component of water over the entire spectral window in Figure 6. The wavelength dependence of A_l in eq 4 can be complex since not just ϵ, but also k_{rd} and k, can vary as a function of 4-methoxybenzene binding configuration at the SWCNT surface.

DOI: 10.1021/acsnano.8b02909
ACS Nano 2018, 12, 8060−8070

CONCLUSION

In summary, we have observed significant dependence of defect-state relaxation dynamics on emission state energy and solvent environment in functionalized SWCNTs. The wavelength dependence of the dynamics originates in thermal detrapping of excitons from defect sites to regenerate diffusive band-edge excitons. This process is fundamental to the observation of photon upconversion in functionalized SWCNTs. Analysis of the energy dependence of the dynamics demonstrates that the detrapping rate can be competitive with other population loss or relaxation pathways. The strong solvent dependence of the dynamics is evidence of nonradiative exciton relaxation through an EVET, which we introduce as an additional mechanism for excited-state relaxation in SWCNTs. EVET rates are dependent on spectral overlap between defect-state electronic transitions with the near-IR solvent absorption due to vibrational overtones and combination modes. Of the solvents studied, H_2O is found to be the most effective medium for EVET due to its strong and continuous absorption throughout the defect-state emission region. Thus, in addition to multiphonon decay, demonstrated in earlier work to be an important pathway for defect-state relaxation,[14,21] thermal detrapping and EVET are shown here to be competing decay channels. These processes act on similar time scales and are tunable by solvent choice. Defect-state dynamics thus can be readily tailored by environmental control. Interestingly, the short decay component is found to be independent of solvent. This observation is consistent with our earlier interpretation of the defect-state dynamics as being defined by a redistribution of bright and dark state populations happening on short time scales, while relaxation of the entire defect-state manifold to the ground state occurs on long time scales.[14] This interpretation is further supported by the behavior of the amplitudes of the decay components, also dependent on both emission wavelength and solvent. These in-depth studies of defect-state dynamics add significantly to our understanding of the associated relaxation mechanisms and electronic structure, required for developing a complete picture of defect-state photophysics. The results also provide additional insight into how we may modulate environmental interactions toward optimizing PL quantum yields and controlling the dynamics associated with defect-state quantum emission.

METHODS

Preparation of Functionalized SWCNT Samples. Samples highly enriched in (6,5) chirality SWCNTs in 1% sodium deoxycholate (DOC) were prepared from CoMoCAT SG65i (Sigma-Aldrich) starting material by using a two-step aqueous two-phase extraction process, as described previously.[14,46] Functionalization of the (6,5)-enriched sample with 4-methoxybenzene proceeded by first exchanging the DOC-wrapped samples into 1% (w/v) sodium dodecyl sulfate (SDS) by ultrafiltration. A volume of 50 μL of doping solution (0.1 mg/mL of 4-methoxybenzene diazonium tetrafluoroborate salt in DI water) was then added to 1 mL of the SWCNT solution, adjusted to a concentration for which an optical density of ~0.1 is obtained at the E_{11} absorption peak. The reaction is monitored via PL spectroscopy and the progress is stopped after attaining the desired defect-state PL level by exchanging the samples into 1% (w/v) DOC. This initially functionalized sample serves as the sole source of material for subsequent exchange into the polymer wrapping and different solvent systems.

SWCNT Polymer Wrapping and Exchange into Varying Solvents. Aqueous suspensions of DOC-wrapped (6,5) SWCNT, prefunctionalized with 4-methoxybenzene, were wrapped with the S-PBn(b)-Ph_4 polymer as follows. The complete synthesis of S-PBn(b)-Ph_4 is described in the Supporting Information. A volume of 12 mL of an aqueous suspension of functionalized-[(6,5) SWCNTs] was added over the course of 3 h to a 10 mL solution of S-PBn(b)-Ph_4 (3:7 MeOH/H_2O, 0.5 mg/mL). The mixture was stirred overnight and was exchanged into a 5 mM carbonate/15 mM NaCl buffer (pH ~ 9) using a Microcon centrifugal filter YM-100 (Millipore, Bedford, MA). Free, unbound polymers were removed via gel permeation chromatography: a 2 mL polymer/SWCNT solution (SWCNT concentration of ~0.5 mg/mL) was injected into a series of two preparative columns (160 × 16 mm each) loaded with sephacryl-based separatory medium connected in the order of S-500 (Sigma-Aldrich; MW fractionation range 40−20 000 kDa (dextran) and S-200 (Sigma-Aldrich; MW fractionation range 1−80 kDa (dextran)), mounted on a GE/ÄKTApurifier HPLC system (GE Healthcare Bio-Science AB, Björkgatan, Uppsala, Sweden), and eluted with a 5 mM carbonate/15 mM NaCl buffer in 3:7 MeOH:H_2O at a flow rate of 1 mL/min; three-wavelength detection (for all samples, carbon nanotubes were detected at 580 nm; phenylene-based polymers were detected at 315 and 440 nm) was used to identify fractions that did not contain SWCNTs (see the Supporting Information). The fractions were collected as 1 mL aliquots; the polymer/SWCNT fractions eluted at an earlier time (18−25 min range) followed by the free, unbound polymers (26−48 min range). We note that this chromatography procedure also serves to narrow the length distribution of the collected polymer/SWCNT fraction, providing average length distributions of 700 ± 50 nm.[47] Polymer/SWCNT-containing fractions (eluting over an 18−25 min range) were collected together and desalted via centrifuging through a Microcon centrifugal filter YM-100 (Millipore, Bedford, MA) while washing (~4 × 5 mL) with aqueous solvent mixture containing no salt. The polymer-wrapped SWCNT are exchanged into various solvent systems as follows (see also Scheme 1 and Figures S6−S8, Supporting Information):

[H_2O]. The desalted SWCNT solution was partitioned between two vials. The volume of each was adjusted to 6 mL of H_2O and bath sonicated for 30 min.

[D_2O]. From the previously prepared SWCNT H_2O solution, 1 mL was placed in a separate vial under vacuum for 24 h. The resulting solid was taken up in 1 mL of D_2O and bath sonicated for 30 min.

[MeOH]. To 4 mL of the obtained SWCNT H_2O solution, 150 μL of 15-C-5 crown ether was added in order to complex the sodium cations, after which the solvent was removed under vacuum for 24 h. The resulting sticky green solid was redissolved in 4 mL of MeOH and bath sonicated for 30 min.

[DMF]. To disperse the polymer-wrapped SWCNT in DMF, 1 mL of the obtained SWCNT MeOH solution was placed under vacuum for 24 h. The sticky green solid was then dissolved in 1 mL of DMF and bath sonicated for 30 min.

[THF]. Here 20 mg of amphiphilic counterion **S-8** (see Supporting Information Figure S8) was dissolved in 5 mL of a mixture of 1:1 DMSO/MeOH at 60 °C, and cannula transferred to 2 mL of the SWCNT MeOH solution. A fluffy green solid precipitated immediately and the reaction mixture was stirred for 1 h at 60 °C, then cooled to room temperature. The resulting precipitate was filtered through a 0.20 μm hydrophobic PTFE membrane (Millipore-FGLP), and the filtered solid was washed with 7:3 THF:MeOH in order to remove the excess unmetathesized **S-8**. The resulting solid was taken up in 1.2 mL of THF and bath sonicated for 30 min.

[THF:Toluene]. To prepare the SWCNT THF/toluene (20:80) solution, 0.2 mL of the SWCNT THF solution was diluted with 0.8 mL of toluene and bath sonicated for 30 min.

Optical Measurements. Solution-phase ensemble photoluminescence spectra were obtained using a Horiba Nanolog spectrofluorometer incorporating an 800 nm long-pass filter in the collection beam path. PL lifetimes were obtained using tunable pulsed Ti:sapphire laser excitation (150 fs pulsewidth, 90 MHz repetition rate). Laser excitation at 840 nm (at the (6,5) SWCNT phonon sideband) was coupled into an inverted microscope body and focused

DOI: 10.1021/acsnano.8b02909
ACS Nano 2018, 12, 8060−8070

onto the sample with an infrared objective (Olympus, 50X, NA = 0.65). PL was collected by the objective and filtered through a 10 nm bandpass tunable filter that was tuned across the defect-state emission wavelength range. The selected defect-state PL band was directed onto a superconducting nanowire detector via an infrared pellicle beam splitter (Thorlabs BP133). HydraHarp 400 (Picoquant) time correlated single photon counting electronics were used to record the PL transients. Transients were reconvolution fit (accounting for the instrument response function (IRF)) to a biexponential decay where PL intensity $I(t) = A_s e^{-t/\tau_s} + A_l e^{-t/\tau_l}$.[14] Representative transients obtained at four different excitation wavelengths and for two different solvent systems (H_2O and THF/toluene) are available in the Supporting Information, Figures S9 and S10.

Computational Methodology. Pristine (6,5) single-walled carbon nanotube segments of ~12 nm (generated from 3 unit-cells) in length (approximately 3 unit-cells) were generated using VMD 1.9.3 software.[48] These finite SWCNTs must first be capped in order to replicate the electronic structure of an infinite-length system. We used the capping scheme (hydrogen atoms at every terminal carbon atom) that was previously developed for (6,5) tubes.[49,50] The systems were then functionalized with aryl-based functional groups at approximately the center of the SWCNT. The functionalization schemes generated are presented in a previous report.[35] To avoid the formation of open-shelled systems, a hydrogen atom was placed in positions either adjacent to the functional group (ortho) or across the hexagonal ring from the functional group (para) as previously described.[18,35]

Time-dependent density functional theory (TDDFT) was used to optimize excited state geometries of each system using the CAM-B3LYP density functional, as has been previously shown to reasonably determine electron localization in functionalized SWCNT systems[51] and reasonably agrees with experiment.[52,53] Since optical energies in these systems have been previously shown to be independent of basis set size,[35] the minimal STO-3G basis set[54] was used. Our TDDFT calculations provide the optical transition energies and intensities (oscillator strengths) required for estimating radiative lifetimes τ as

$$\tau = \frac{2\pi c^3 \varepsilon_0 m_e}{f_{ij}\omega^2 e^2} \quad (5)$$

where c is the speed of light, ε_0 is the permittivity of free space, m_e is the mass of an electron, e is the elementary charge, and f_{ij} and ω are the oscillator strength and frequency of the transition, respectively, calculated with TDDFT as implemented in the Gaussian09 software package.[55] This approach is very similar to previous modeling of lifetimes.[56,57] Reorganization energies were calculated with the following equations:

$$\Delta E_1 = \text{reorganization energy in ground state} = E_{S1}^{SP} - E_{S0}^{SP} \quad (6)$$

$$\Delta E_2 = \text{reorganization energy in excited state} = E_{abs} - (E_{emis} + \Delta E_1) \quad (7)$$

where ΔE_1 and ΔE_2 are the reorganization energies in the ground and excited state respectively, E_{S1}^{SP} and E_{S0}^{SP} are the total energies of the first excited and ground states, respectively, at optimal geometries, and E_{abs} and E_{emis} are the vertical transition energies from the ground and excited state geometries, respectively. A graphical representation of these parameters is found in Figure S3, Supporting Information.

ASSOCIATED CONTENT

Supporting Information

The Supporting Information is available free of charge on the ACS Publications website at DOI: 10.1021/acsnano.8b02909.

Morphological characteristics of polymer-SWCNT superstructure composites; tabulation of solvent dielectric constant and solvent-dependent position of PL emission from band-edge exciton (E11) and defect states (E_{11}* and E_{11}*$^-$); demonstration of reconvolution fitting of defect-state PL decay and additional examples of PL decay data; schematic of the potential energy surface and computation parameters, tabulation of TDDFT calculation results for energies of absorption and emission, transition dipoles, radiative lifetimes, defect-state excitation and emission for 4-mexthoxybenzene-functionalized (6,5) SWCNTs; discussion about the dependence of radiative relaxation rate on electronic state, corresponding oscillator strength and solvent dielectric constant; development of theoretical description for EVET mechanism in SWCNTs; complete details on synthesis of the S-PBn(b)-Ph_4 wrapping polymer (PDF)

AUTHOR INFORMATION

Corresponding Author

*E-mail: skdoorn@lanl.gov.

ORCID

Xiaowei He: 0000-0002-4982-8250
Kirill A. Velizhanin: 0000-0003-0645-1112
George Bullard: 0000-0002-3725-9046
Jean-Hubert Olivier: 0000-0003-0978-4107
Nicolai F. Hartmann: 0000-0002-4174-532X
Brendan J. Gifford: 0000-0002-4116-711X
Svetlana Kilina: 0000-0003-1350-2790
Sergei Tretiak: 0000-0001-5547-3647
Han Htoon: 0000-0003-3696-2896
Michael J. Therien: 0000-0003-4876-0036
Stephen K. Doorn: 0000-0002-9535-2062

Present Address

○J.-H.O.: Department of Chemistry, University of Miami, Coral Gables, Florida 33146-0431.

Author Contributions

#X.H. and K.A.V.: Equal contributions.

Notes

The authors declare no competing financial interest.

ACKNOWLEDGMENTS

This work was conducted in part at the Center for Integrated Nanotechnologies, a U.S. Department of Energy, Office of Basic Energy Sciences user facility, and supported in part by Los Alamos National Laboratory (LANL) Directed Research and Development funds. Y.B. and G.B. are grateful to the Fitzpatrick Institute for Photonics at Duke University for John T. Chambers Scholars Awards. G.B., Y.B., J.-H.O., and M.J.T acknowledge the Division of Chemical Sciences, Geosciences, and Biosciences, Office of Basic Energy Sciences, of the U.S. Department of Energy through Grant DE-SC0001517, for research support.

REFERENCES

(1) Ghosh, S.; Bachilo, S. M.; Simonette, R. A.; Beckingham, K. M.; Weisman, R. B. Oxygen Doping Modifies Near-infrared Band Gaps in Fluorescent Single-Walled Carbon Nanotubes. *Science* **2010**, *330*, 1656−1659.

(2) Piao, Y. M.; Meany, B.; Powell, L. R.; Valley, N.; Kwon, H.; Schatz, G. C.; Wang, Y. H. Brightening of Carbon Nanotube Photoluminescence Through the Incorporation of sp^3 Defects. *Nat. Chem.* **2013**, *5*, 840−845.

DOI: 10.1021/acsnano.8b02909
ACS Nano 2018, 12, 8060−8070

(3) Kwon, H.; Furmanchuk, A. O.; Kim, M.; Meany, B.; Guo, Y.; Schatz, G. C.; Wang, Y. Molecularly Tunable Fluorescent Quantum Defects. *J. Am. Chem. Soc.* **2016**, *138*, 6878−6885.
(4) O'Connell, M. J.; Bachilo, S. M.; Huffman, C. B.; Moore, V.; Strano, M. S.; Haroz, E. H.; Rialon, K. L.; Boul, P. J.; Noon, W. H.; Kittrell, C.; Ma, J.; Hauge, R. H.; Weisman, R. B.; Smalley, R. E. Band Gap Fluorescence from Individual Single-Walled Carbon Nanotubes. *Science* **2002**, *297*, 593−596.
(5) Kwon, H.; Kim, M.; Meany, B.; Piao, Y.; Powell, L. R.; Wang, Y. Optical Probing of Local pH and Temperature in Complex Fluids with Covalently Functionalized Semiconducting Carbon Nanotubes. *J. Phys. Chem. C* **2015**, *119*, 3733−3739.
(6) Shiraki, T.; Onitsuka, H.; Shiraishi, T.; Nakashima, N. Near Infrared Photoluminescence Modulation of Single-Walled Carbon Nanotubes Based on a Molecular Recognition Approach. *Chem. Commun.* **2016**, *52*, 12972−12975.
(7) Akizuki, N.; Aota, S.; Mouri, S.; Matsuda, K.; Miyauchi, Y. Efficient Near-Infrared Up-Conversion Photoluminescence in Carbon Nanotubes. *Nat. Commun.* **2015**, *6*, 8920.
(8) Maeda, Y.; Minami, S.; Takehana, Y.; Dang, J.-S.; Aota, S.; Matsuda, K.; Miyauchi, Y.; Yamada, M.; Suzuki, M.; Zhao, R.-S.; et al. Tuning of the Photoluminescence and Up-Conversion Photoluminescence Properties of Single-Walled Carbon Nanotubes by Chemical Functionalization. *Nanoscale* **2016**, *8*, 16916−16921.
(9) Aota, S.; Akizuki, N.; Mouri, S.; Matsuda, K.; Miyauchi, Y. Upconversion Photoluminescence Imaging and Spectroscopy of Individual Single-Wall Carbon Nanotubes. *Appl. Phys. Express* **2016**, *9*, 045103.
(10) Ma, X.; Hartmann, N. F.; Baldwin, J. K. S.; Doorn, S. K.; Htoon, H. Room-Temperature Single-Photon Generation from Solitary Dopants of Carbon Nanotubes. *Nat. Nanotechnol.* **2015**, *10*, 671−675.
(11) He, X.; Hartmann, N. F.; Ma, X.; Kim, Y.; Ihly, R.; Blackburn, J. L.; Gao, W.; Kono, J.; Yomogida, Y.; Hirano, A.; Tanaka, T.; Kataura, H.; Htoon, H.; Doorn, S. K. Tunable Room-Temperature Single-Photon Emission at Telecom Wavelengths from sp^3 Defects in Carbon Nanotubes. *Nat. Photonics* **2017**, *11*, 577−582.
(12) Miyauchi, Y.; Iwamura, M.; Mouri, S.; Kawazoe, T.; Ohtsu, M.; Matsuda, K. Brightening of Excitons in Carbon Nanotubes on Dimensionality Modification. *Nat. Photonics* **2013**, *7*, 715−719.
(13) Hartmann, N. F.; Yalcin, S. E.; Adamska, L.; Hároz, E. H.; Ma, X.; Tretiak, S.; Htoon, H.; Doorn, S. K. Photoluminescence Imaging of Solitary Dopant Sites in Covalently Doped Single-wall Carbon Nanotubes. *Nanoscale* **2015**, *7*, 20521−20530.
(14) Hartmann, N. F.; Velizhanin, K. A.; Haroz, E. H.; Kim, M.; Ma, X.; Wang, Y.; Htoon, H.; Doorn, S. K. Photoluminescence Dynamics of Aryl sp3 Defect States in Single-Walled Carbon Nanotubes. *ACS Nano* **2016**, *10*, 8355−8365.
(15) Ma, X.; Adamska, L.; Yamaguchi, H.; Yalcin, S. E.; Tretiak, S.; Doorn, S. K.; Htoon, H. Electronic Structure and Chemical Nature of Oxygen Dopant States in Carbon Nanotubes. *ACS Nano* **2014**, *8*, 10782−10789.
(16) Ohfuchi, M. Ab Initio Study on Oxygen Doping of (5,4), (6,4), (6,5), and (8,6) Carbon Nanotubes. *J. Phys. Chem. C* **2015**, *119*, 13200−13206.
(17) Ramirez, J.; Mayo, M. L.; Kilina, S.; Tretiak, S. Electronic Structure and Optical Spectra of Semiconducting Carbon Nanotubes Functionalized by Diazonium Salts. *Chem. Phys.* **2013**, *413*, 89−101.
(18) He, X.; Gifford, B. J.; Hartmann, N. F.; Ihly, R.; Ma, X.; Kilina, S. V.; Luo, Y.; Shayan, K.; Strauf, S.; Blackburn, J. L.; Tretiak, S.; Doorn, S. K.; Htoon, H. Low-Temperature Single Carbon Nanotube Spectroscopy of sp^3 Quantum Defects. *ACS Nano* **2017**, *11*, 10785−10796.
(19) Iwamura, M.; Akizuki, N.; Miyauchi, Y.; Mouri, S.; Shaver, J.; Gao, Z.; Cognet, L.; Lounis, B.; Matsuda, K. Nonlinear Photoluminescence Spectroscopy of Carbon Nanotubes with Localized Exciton States. *ACS Nano* **2014**, *8*, 11254−11260.
(20) Hertel, T.; Himmelein, S.; Ackermann, T.; Stich, D.; Crochet, J. Diffusion Limited Photoluminescence Quantum Yields in 1-D Semiconductors: Single-Wall Carbon Nanotubes. *ACS Nano* **2010**, *4*, 7161−7168.
(21) Perebeinos, V.; Avouris, P. Phonon and Electronic Nonradiative Decay Mechanisms of Excitons in Carbon Nanotubes. *Phys. Rev. Lett.* **2008**, *101*, 057401.
(22) Kim, M.; Adamska, L.; Hartmann, N. F.; Kwon, H.; Velizhanin, K. A.; Piao, Y.; Powell, L. R.; Meany, B.; Doorn, S. K.; Tretiak, S.; Wang, Y. Fluorescent Carbon Nanotube Defects Manifest Substantial Vibrational Reorganization. *J. Phys. Chem. C* **2016**, *120*, 11268−11276.
(23) Walsh, A. G.; Vamivakas, A. N.; Yin, Y.; Cronin, S. B.; Unlu, M. S.; Goldberg, B. B.; Swan, A. K. Screening of Excitons in Single Suspended Carbon Nanotubes. *Nano Lett.* **2007**, *7*, 1485−1488.
(24) Ohno, Y.; Iwasaki, S.; Murakami, Y.; Kishimoto, S.; Maruyama, S.; Mizutani, T. Excitonic Transitions in Single-Walled Carbon Nanotubes: Dependence on Environmental Dielectric Constant. *Phys. Status Solidi B* **2007**, *244*, 4002−4005.
(25) Wenseleers, W.; Vlasov, I. I.; Goovaerts, E.; Obraztsova, E. D.; Lobach, A. S.; Bouwen, A. Efficient Isolation and Solubilization of Pristine Single-Walled Carbon Nanotubes in Bile Salt Micelles. *Adv. Funct. Mater.* **2004**, *14*, 1105−1112.
(26) Zheng, M.; Jagota, A.; Semke, E. D.; Diner, B. A.; Mclean, R. S.; Lustig, S. R.; Richardson, R. E.; Tassi, N. G. DNA-Assisted Dispersion and Separation of Carbon Nanotubes. Nat. *Nat. Mater.* **2003**, *2*, 338−342.
(27) Nish, A.; Hwang, J.-Y.; Doig, J.; Nicholas, R. J. Highly Selective Dispersion of Single-Walled Carbon Nanotubes Using Aromatic Polymers. *Nat. Nanotechnol.* **2007**, *2*, 640−646.
(28) Deria, P.; Sinks, L. E.; Park, T. H.; Tomezsko, D. M.; Brukman, M. J.; Bonnell, D. A.; Therien, M. J. Phase Transfer Catalysts Drive Diverse Organic Solvent Solubility of Single-Walled Carbon Nanotubes Helically Wrapped by Ionic Semiconducting Polymers. *Nano Lett.* **2010**, *10*, 4192−4199.
(29) Larsen, B. A.; Deria, P.; Holt, J. M.; Stanton, I. N.; Heben, M. J.; Therien, M. J.; Blackburn, J. L. Effect of Solvent Polarity and Electrophilicity on Quantum Yields and Solvatochromic Shifts of Single-Walled Carbon Nanotube Photoluminescence. *J. Am. Chem. Soc.* **2012**, *134*, 12485−12491.
(30) Rosario-Canales, M. R.; Deria, P.; Therien, M. J.; Santiago-Avilés, J. J. Composite Electronic Materials Based on Poly(3,4-propylenedioxythiophene) and Highly Charged Poly(aryleneethynylene)-Wrapped Carbon Nanotubes for Supercapacitors. *ACS Appl. Mater. Interfaces* **2012**, *4*, 102−109.
(31) Olivier, J.-H.; Deria, P.; Park, J.; Kumbhar, A.; Andrian-Albescu, M.; Therien, M. J. Ionic Self-Assembly Provides Dense Arrays of Individualized, Aligned Single Walled Carbon Nanotubes. *Angew. Chem., Int. Ed.* **2013**, *52*, 13080−13085.
(32) Deria, P.; Olivier, J.-H.; Park, J.; Therien, M. J. Potentiometric, Electronic, and Transient Absorptive Spectroscopic Properties of Oxidized Single-Walled Carbon Nanotubes Helically Wrapped by Ionic, Semiconducting Polymers in Aqueous and Organic Media. *J. Am. Chem. Soc.* **2014**, *136*, 14193−14199.
(33) Deria, P.; Von Bargen, C. D.; Olivier, J.-H.; Kumbhar, A. S.; Saven, J. G.; Therien, M. J. Single-Handed Helical Wrapping of Single-Walled Carbon Nanotubes by Chiral Ionic Semiconducting Polymers. *J. Am. Chem. Soc.* **2013**, *135*, 16220−16234.
(34) Bai, Y. S.; Olivier, J. H.; Bullard, G.; Liu, C. R.; Therien, M. J. Dynamics of Charge Excitons in Electronically and Morphologically Homogeneous Single-Walled Carbon Nanotubes. *Proc. Natl. Acad. Sci. U. S. A.* **2018**, *115*, 674−679.
(35) Gifford, B. J.; Kilina, S.; Htoon, H.; Doorn, S. K.; Tretiak, S. Exciton Localization and Optical Emission in Aryl-Functionalized Carbon Nanotubes. *J. Phys. Chem. C* **2018**, *122*, 1828−1838.
(36) Berestetskii, V. B., Lifshitz, E. M.; Pitaevskii, L. P. *Quantum Electrodynamics*, 2nd ed.; Pergamon: London, 1982; Vol. 4.
(37) Perebeinos, V.; Tersoff, J.; Avouris, P. Radiative Lifetime of Excitons in Carbon Nanotubes. *Nano Lett.* **2005**, *5*, 2495−2499.
(38) Sarpkaya, I.; Zhang, Z.; Walden-Newman, W.; Wang, X.; Hone, J.; Wong, C. W.; Strauf, S. Prolonged Spontaneous Emission and

DOI: 10.1021/acsnano.8b02909
ACS Nano 2018, 12, 8060−8070

Dephasing of Localized Excitons in Air-Bridged Carbon Nanotubes. Nat. *Nat. Commun.* **2013**, *4*, 2152.
(39) Aharoni, A.; Oron, D.; Banin, U.; Rabani, E.; Jortner, J. Long-Range Electronic-to-Vibrational Energy Transfer from Nanocrystals to Their Surrounding Matrix Environment. *Phys. Rev. Lett.* **2008**, *100*, 057404.
(40) Wen, Q.; Kershaw, S. V.; Kalytchuk, S.; Zhovtiuk, O.; Reckmeier, C.; Vasilevskiy, M. I.; Rogach, A. L. Impact of D_2O/H_2O Solvent Exchange on the Emission of HgTe and CdTe Quantum Dots: Polaron and Energy Transfer Effects. *ACS Nano* **2016**, *10*, 4301−4311.
(41) Homma, Y.; Chiashi, S.; Yamamoto, T.; Kono, K.; Matsumoto, D.; Shitaba, J.; Sato, S. Photoluminescence measurements and molecular dynamics simulations of water adsorption on the hydrophobic surface of a carbon nanotube in water vapor. *Phys. Rev. Lett.* **2013**, *110*, 157402.
(42) Vijayaraghavan, V.; Wong, C. H. Torsional Characteristic of Single Walled Carbon Nanotube with Water Interactions by Using Molecular Dynamics Simulations. *Nano-Micro Lett.* **2014**, *6*, 268−279.
(43) Kedenburg, S.; Vieweg, M.; Gissibl, T.; Giessen, H. Linear Refractive Index and Absorption Measurements on Nonlinear Optical Liquids in the Visible and Near-Infrared Spectral Region. *Opt. Mater. Express* **2012**, *2*, 1588−1611.
(44) Duque, J. G.; Oudjedi, L.; Crochet, J. J.; Tretiak, S.; Lounis, B.; Doorn, S. K.; Cognet, L. Mechanism of Electrolyte Induced Brightening of Single-Wall Carbon Nanotubes. *J. Am. Chem. Soc.* **2013**, *135*, 3379−3382.
(45) Gluckert, J. T.; Adamska, L.; Schinner, W.; Hofmann, M. S.; Doorn, S. K.; Tretiak, S.; Hogele, A. Dipolar and Charged Localized Excitons in Carbon Nanotubes. 2017, arXiv:1706.08347. arXiv.org e-Print archive.
(46) Subbaiyan, N. K.; Cambre, S.; Parra-Vasquez, A. N. G.; Haroz, E. H.; Doorn, S. K.; Duque, J. G. Role of Surfactant and Salt in Aqueous Two-Phase Separation of Carbon Nanotubes toward Simple Chirality Isolation. *ACS Nano* **2014**, *8*, 1619−1628.
(47) Park, J.; Deria, P.; Olivier, J.-H.; Therien, M. J. Fluence-Dependent Singlet Exciton Dynamics in Length-Sorted Chirality-Enriched Single-Walled Carbon Nanotubes. *Nano Lett.* **2014**, *14*, 504−511.
(48) Humphrey, W.; Dalke, A.; Schulten, K. VMD − Visual Molecular Dynamics. *J. Mol. Graphics* **1996**, *14*, 33−38.
(49) Kilina, S.; Tretiak, S. Excitonic and Vibrational Properties of Single-Walled Semiconducting Carbon Nanotubes. *Adv. Funct. Mater.* **2007**, *17*, 3405−3420.
(50) Sharma, A.; Gifford, B. J.; Kilina, S. Tip Functionalization of Finite Single-Walled Carbon Nanotubes and Its Impact on the Ground and Excited State Electronic Structure. *J. Phys. Chem. C* **2017**, *121*, 8601−8612.
(51) Adamska, L.; Nazin, G. V.; Doorn, S. K.; Tretiak, S. Self-Trapping of Charge Carriers in Semiconducting Carbon Nanotubes: Structural Analysis. *J. Phys. Chem. Lett.* **2015**, *6*, 3873−3879.
(52) Kilina, S.; Badaeva, E.; Piryatinski, A.; Tretiak, S.; Saxena, A.; Bishop, A. R. Bright and Dark Excitons in Semiconductor Carbon Nanotubes: Insights from Electronic Structure Calculations. *Phys. Chem. Chem. Phys.* **2009**, *11*, 4113−4123.
(53) Kilina, S.; Kilin, D.; Tretiak, S. Light-Driven and Phonon-Assisted Dynamics in Organic and Semiconductor Nanostructures. *Chem. Rev.* **2015**, *115*, 5929−5978.
(54) Hehre, W. J.; Stewart, R. F.; Pople, J. A. Self-Consistent Molecular-Orbital Methods. I. Use of Gaussian Expansions of Slater-Type Atomic Orbitals. *J. Chem. Phys.* **1969**, *51*, 2657−2664.
(55) Frisch, M. J.; Trucks, G. W.; Schlegel, H. B.; Scuseria, G. E.; Robb, M. A.; Cheeseman, J. R.; Scalmani, G.; Barone, V.; Mennucci, B.; Petersson, G. A.; Nakatsuji, H.; Caricato, M.; Li, X.; Hratchian, H. P.; Izmaylov, A. F.; Bloino, J.; Zheng, G.; Sonnenberg, J. L.; Hada, M.; Ehara, M.; Toyota, K.; et al. *Gaussian 09*; Gaussian, Inc.: Wallingford, CT, 2009.
(56) Chen, J.; Schmitz, A.; Kilin, D. S. Computational Simulation of the P-n Doped Silicon Quantum Dot. *Int. J. Quantum Chem.* **2012**, *112*, 3879−3888.
(57) Kilina, S.; Ramirez, J.; Tretiak, S. Brightening of the Lowest Exciton in Carbon Nanotubes *via* Chemical Functionalization. *Nano Lett.* **2012**, *12*, 2306−2312.

DOI: 10.1021/acsnano.8b02909
ACS Nano 2018, 12, 8060−8070